Nanoscale Research Letters

NANO EXPRESS

Open Access

Conversation from antiferromagnetic $MnBr_2$ to ferromagnetic Mn_3Br_8 monolayer with large MAE

Y. Hu[1], S. Jin[2], Z. F. Luo[1], H. H. Zeng[1], J. H. Wang[1] and X. L. Fan[1*]

Abstract

A pressing need in low energy spintronics is two-dimensional (2D) ferromagnets with Curie temperature above the liquid-nitrogen temperature (77 K), and sizeable magnetic anisotropy. We studied Mn_3Br_8 monolayer which is obtained via inducing Mn vacancy at 1/4 population in $MnBr_2$ monolayer. Such defective configuration is designed to change the coordination structure of the Mn-d^5 and achieve ferromagnetism with sizeable magnetic anisotropy energy (MAE). Our calculations show that Mn_3Br_8 monolayer is a ferromagnetic (FM) half-metal with Curie temperature of 130 K, large MAE of − 2.33 meV per formula unit, and atomic magnetic moment of $13/3\mu_B$ for the Mn atom. Additionally, Mn_3Br_8 monolayer maintains to be FM under small biaxial strain, whose Curie temperature under 5% compressive strain is 160 K. Additionally, both biaxial strain and carrier doping make the MAE increases, which mainly contributed by the magneto-crystalline anisotropy energy (MCE). Our designed defective structure of $MnBr_2$ monolayer provides a simple but effective way to achieve ferromagnetism with large MAE in 2D materials.

Keywords: First-principles calculations, Ferromagnetism, Two-dimensional (2D) materials, Magnetic anisotropy energy (MAE)

Introduction

Spintronics, exploiting the electron spin and the associated magnetic moment, has attracted extensive attention during the past few decades [1], because of its unique advantages over charge-based devices. The recent realization of two-dimensional (2D) ferromagnets with long-range magnetic ordering at finite temperature [2, 3] is of great significance for nanoscale spintronics and related applications and inspires tremendous efforts in investigations and fabrications of 2D ferromagnets [4–9].

The first two 2D ferromagnets with atomic-thickness was achieved in 2017, that is monolayer CrI_3 [2] and bilayer $Cr_2Ge_2Te_6$ [3]. Unfortunately, both their Curie temperatures are lower than the liquid-nitrogen temperature (77 K), which limits their realistic applications. Besides the Curie temperature, sizeable magnetic anisotropy and magnetic moment are also indispensable for practical application. Large magnetic anisotropy energy (MAE) implies the benefit for the magnetic ordering against the heat fluctuation, and the possibility to reduce the grain size per bit of information; small MAE may results in super-paramagnetic rather than ferromagnetic. Large magnetic moment provides higher sensitivity, higher efficiency, and higher density for spintronics. Heavy elements are more likely to bring in large MAE due to their strong spin-orbital coupling (SOC) effect [10]. A series of 2D FM materials composed of heavy elements have been predicted having large MAE, such as CrI_3 [11], CrAs [12], CrSeI [13], $CrSiTe_3$ [14], $CrWI_6$ [15], $FeBr_2$ and FeI_2 monolayers [16]. Additionally, the local magnetic moment on Mn atom of MXenes Mn_2NF_2 and

*Correspondence: xlfan@nwpu.edu.cn
[1] State Key Laboratory of Solidification Processing, Center for Advanced Lubrication and Seal Materials, School of Material Science and Engineering, Northwestern Polytechnical University, 127 YouYi Western Road, Xi'an 710072, Shaanxi, China
Full list of author information is available at the end of the article

$Mn_2N(OH)_2$ is 4.5μ_B per Mn atom [17], which is the largest among the reported FM 2D materials.

Since CrI_3 monolayer has been successfully synthesized, transition-metal halides have attracted much attentions [18–27]. Spin Seeback effect has been observed in bilayer MnF_2 [20]; few layers of CrI_3 has been implemented into the magnetic tunneling junctions (MTJ) [21]; $NiCl_3$ monolayer has been predicted to be a novel Dirac spin-gapless semiconductor (SGS) [22]. Particularly, $MnBr_2$ monolayer is antiferromagnetic with 0.25 meV MAE along the perpendicular direction to the plane based on the first-principles calculations [16]; Mn^{2+} ions are in the d^5 high-spin state with magnetic moment of 5μ_B [16, 26]. These results imply the potentials of $MnBr_2$ as monolayer ferromagnet with large magnetic moment. The key problem is how to convert the AFM coupling between Mn ions into FM coupling.

Significant density of Mn vacancy was observed experimentally in $LaMnO_3$ thin films [28], and the concentration of defects can be controlled by regulating the synthesis process deliberately via irradiation of high energy particles, or chemical etching [29]. In this context, we designed the Mn_3Br_8 monolayer by inducing single Mn vacancy to $MnBr_2$ monolayer. The vacancy changes the coordination structure of the Mn atom and breaks the d^5 configuration, which may convert the antiferromagnetic coupling into ferromagnetic coupling and bring in large MAE due to the heavy Br atom. As we expect, Mn_3Br_8 monolayer is FM and has large MAE of −2.33 meV per formula unit, the magnetic moment for each Mn atom is 13/3μ_B. Considering the easy introducing of strain via bending flexible substrates [30–33], elongating elastic substrate [33–35], exploiting the thermal expansion mismatch [33, 36], and so on [33], and the effective control of spin polarization via electrostatic doping [37, 38], we also studied the Mn_3Br_8 monolayer under biaxial strain and carrier doping. Our results show that Mn_3Br_8 monolayer maintains to be FM with Curie temperature increasing under small biaxial strain. Plus, both biaxial strain and carrier doping can make the MAE increases.

Computational methods

All the calculations in the present study were performed by adopting the spin-polarized density function theory (DFT) method as implemented in the Vienna *ab-initio* simulation package (VASP) [39]. Interactions between electrons and nuclei were described by the projector augmented wave (PAW) method [40, 41], and the electronic exchange–correlation interactions were described by the Perdew–Burke–Ernzerhof (PBE) functional within the generalized gradient approximation (GGA) method [42]. The Hubbard U terms were adopted to calculate the strong-correlated interaction [43]; an effective on-site coulomb interaction parameter (U) of 4 eV and an exchange energy (J) of 1 eV which was adopted for studying Mn-incorporated 2D materials were used for the Mn-d electrons [44]. The Brillouin zone integration was carried out by adopting the $9 \times 9 \times 1$ k-mesh based on the Monkhorst–Pack scheme [45]. The phonon spectrums were calculated using the Phonopy code [46] which is implemented within the VASP package. A vacuum space of 20 Å was added along the direction perpendicular to the surface of the monolayer to avoid the interaction between the adjacent layers. The cutoff energy for the plane wave basis set was set as 500 eV. The convergence criterion for the total energy and force was set as 1×10^{-6} eV and 0.01 eV/Å, respectively.

Results and discussions

Cleavage energy, ground state, and stability of the $MnBr_2$ monolayer

The optimized lattice constants of bulk $MnBr_2$ are a = b = 3.95 Å, consistent with the previous experimental result ($a = b = 3.87$ Å) [25]. We firstly explored the feasibility of exfoliating $MnBr_2$ monolayer from the bulk $MnBr_2$. Figure 1a presents the well-known, effective, and widely approved method of calculating the cleavage energy [47–49]. Specifically, the cleavage energy was obtained by calculating the variation of the total energy of the ground state with respect to the separation distance d between the two fracture parts as shown in Fig. 1b, the lattice constants of a and b are fixed as the values at the equilibrium state of bulk $MnBr_2$. The interlayer long-range vdW interactions was described by the Grimme's DFT-D2 scheme [50, 51]. The total energy increases with separation distance and then slowly converges as shown in Fig. 1b. The calculated cleavage energy is 0.10 J/m^2, which is smaller compared with the cleavage energy between the two fracture parts of graphite (0.35 J/m^2) [52], demonstrating the feasibility of obtaining $MnBr_2$ monolayer via micro-mechanical exfoliating method.

$MnBr_2$ monolayer has the C_{3v} symmetry as shown in Fig. 1c; each Mn atom is surrounded by 6 neighboring Br atoms, forming an octahedral $[MnBr_6]^{4-}$ unit. As shown in Fig. 2a and b, three possible magnetic configurations, namely non-magnetic (NM), ferromagnetic (FM), and antiferromagnetic (AFM) states are considered. Both high-spin and low-spin states of the Mn ion are considered. Our results show that the Mn ions of FM state are in low-spin with d^1 configuration, while the Mn ions in AFM state are in high-spin with d^5 configuration. The ground state of $MnBr_2$ monolayer is the AFM state, which is more stable than the NM and FM states by 3.91 eV and 0.72 eV per formula unit, respectively (Additional file 1: Table. S1). The MAE is

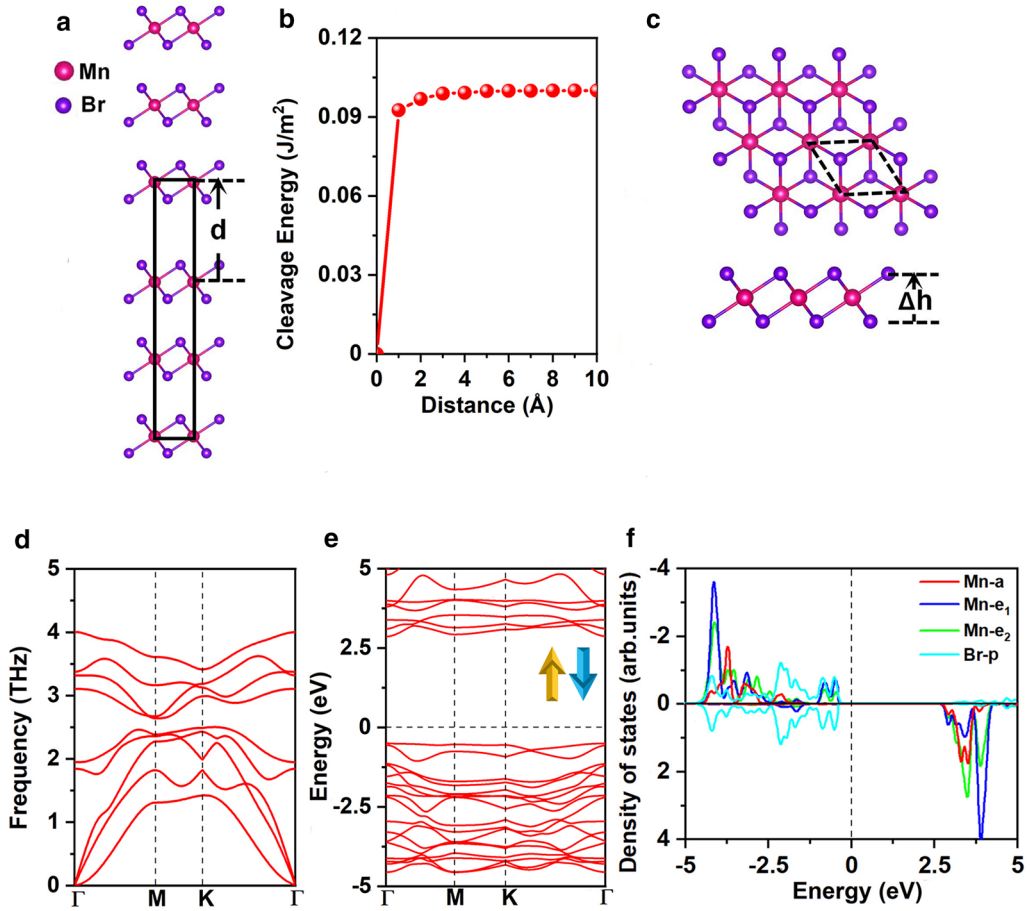

Fig. 1 **a** Bulk model of $MnBr_2$ used to calculate the cleavage energy and **b** the cleavage energy as a function of the separation distance *d* between two fractured parts (the equilibrium interlayer distance is set as 0). **c** Top and side views, **d** phonon spectrum, **e** electronic band structure for both spin channels and **f** projected density of states (PDOS) of Mn-d orbitals and Br-p orbitals for $MnBr_2$ monolayer. Δh represents the vertical distance between two halide planes. The primitive cell is circulated in black dash lines. The Fermi level for band structure and DOS is set as 0 eV

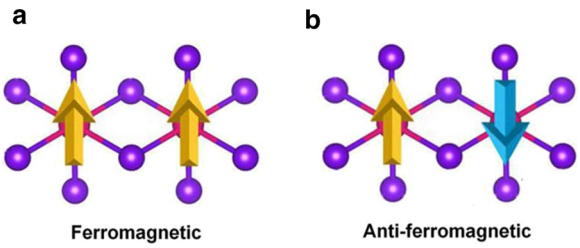

Fig. 2 Schematic diagrams for **a** ferromagnetic and **b** antiferromagnetic configurations for $MnBr_2$ monolayer

0.25 meV, the positive value indicating that the easy magnetization axis is along the out-of-plane directions, agreeing with the previous result [16]. The optimized lattice constants are $a = b = 3.95$ Å, same with the lattice constants of the bulk $MnBr_2$. The Mn-Br bond length is 2.73 Å, and the vertical distance between the two halide planes is 3.03 Å.

The stability of the $MnBr_2$ monolayer was further investigated by calculating the formation energy, phonon spectrum, and elastic constants. The formation energy is calculated as:

$$E_{\text{form}} = E_{\text{MnBr}_2} - E_{\text{Mn}} - 2E_{\text{Br}}$$

where E_{MnBr_2} represents the energy of $MnBr_2$ monolayer, E_{Mn} and E_{Br} are the energies of Mn and Br atoms in their bulk structures, respectively. The calculated E_{form} is -1.87 eV per atom; the negative value means that the formation is exothermic and $MnBr_2$ monolayer is energetical favorable. Plus, our calculated phonon spectrum (Fig. 1d) for $MnBr_2$ monolayer shows no negative frequency in the whole Brillouin zone, indicating dynamically stable. Additionally, the calculated elastic constants

(Additional file 1: Table S2) comply with the Born-Huang criteria [53] of $C_{11} > 0$, $C_{11}C_{22} - C_{12}^2 > 0$ and $C_{66} > 0$, confirming that $MnBr_2$ monolayer is mechanically stable. The calculated in-plane stiffness is 26.98 J/m^2, about 75% of the $MnPSe_3$ (36 J/m^2) [49], and 15% of MoS_2 monolayer (180 J/m^2) [54]. Plus, $MnBr_2$ monolayer demonstrates higher flexibility, and the ability of sustaining larger tensile strain comparing with MoS_2 monolayer (11%) [54]. This may attributes to ionic bonds for $MnBr_2$ monolayer against the covalent bonds of MoS_2 monolayer. The analysis of the deformation related to elastic constants indicates it can withstand its weight (See details in the SI).

The electronic band structure of $MnBr_2$ monolayer is shown in Fig. 1e, it indicates that $MnBr_2$ monolayer is a semiconductor with a direct band gap of 3.35 eV. Both valence band maximum (VBM) and conduction band minimum (CBM) are located at the Γ point. To gain insight of the electronic structures, projected density of states (DOS) for the Mn-d and Br-p orbital are presented in Fig. 1f. The five d orbitals of Mn ion split into $a(d_{z^2})$, $e_1(d_{xz} + d_{yz})$, and $e_2(d_{xy} + d_{x^2-y^2})$ groups according to the C_{3v} symmetry. The bader charge analysis suggests that each Mn atom donates two electrons to the two neighboring Br atoms. Thus, the five d-orbitals in one spin-channel are fully occupied by the five d-electrons of the Mn^{2+} ions. Correspondingly, the two Mn^{2+} ions in the unit cell are in the d^5 high-spin state with the magnetic moment of $5\mu_B/-5\mu_B$, the Br^{1-} ions are in the low-spin state of $4p^6$ with neglectable magnetic moment of $-0.02\mu_B$ (Additional file 1: Fig. S1(a)). According to the Goodenough–Kanamori–Anderson (GKA) rule, such configuration always provides antiferromagnetic coupling [55].

Stability, electronic, and magnetic properties of Mn_3Br_8 monolayer

Mn vacancy was introduced to break the d^5 configuration of the Mn^{2+} ions. Single Mn vacancy is introduced in the $2 \times 2 \times 1$ supercell of $MnBr_2$ monolayer, which gives out the Mn_3Br_8 monolayer. As shown in Fig. 3a, each Mn atom has four nearest neighboring Mn atoms and binds to six Br atoms, forming a distorted octahedral [$MnBr_6$] unit. Five magnetic states (NM, FM, FIM, AFM-1, and AFM-2) shown in Fig. 4 were considered. Our results indicate that the FM state is the ground state, which is more stable than the other four by 9.84 eV, 32.90 meV, 129.85 meV, and 97.65 meV per formula unit, respectively. The optimized lattice constant is still 3.95 Å. Different from $MnBr_2$ monolayer, Mn_3Br_8 monolayer has 2 types of Mn-Br bonds (Fig. 3b). The bonds between Mn atom and the two central Br atoms ($d_{\text{Mn-Br1,2}}$) are 2.76 Å, while the other Mn–Br bonds ($d_{\text{Mn-Br3,4,5,6}}$) are 2.59 Å.

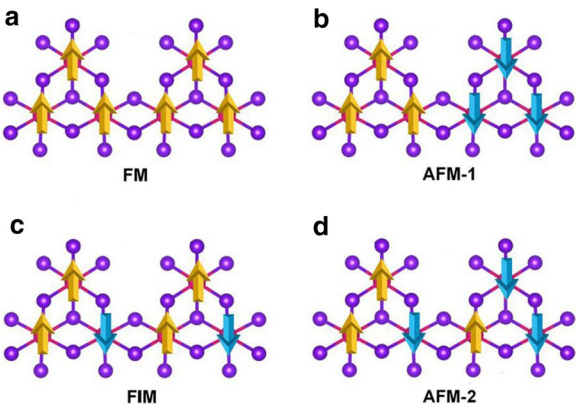

Fig. 4 Schematic diagrams for **a** ferromagnetic, **b** antiferromagnetic-1, **c** ferrimagnetic,and **d** antiferromagnetic-2 configurations for Mn_3Br_8 monolayer

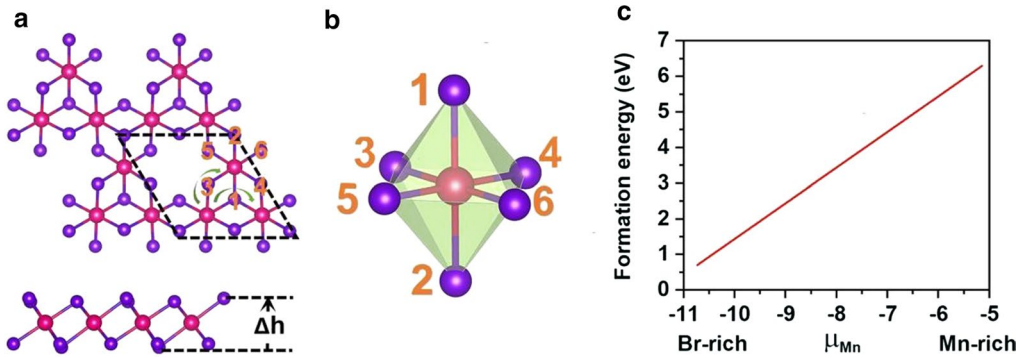

Fig. 3 **a** Top and side views of Mn_3Br_8 monolayer, Δh represents the vertical distance between two halide planes. The primitive cell is circulated in black dash lines; the green arrow lines show two different paths of the super-exchange interaction. **b** Structure of the distorted $MnBr_6$ octahedron. **c** Formation energies for single Mn vacancy as a function of chemical potential of Mn (μMn)

The vertical distance between the two halide planes is 3.33 Å.

To verify the feasibility of inducing Mn vacancy, we firstly calculated the vacancy formation energies under Mn-rich and Br-rich environments via following equations,

$$E_{F(\text{Mn-rich})} = E_{Mn_3Br_8} - (4 \times E_{MnBr_2} - \mu_{\text{Mn-max}})$$

$$E_{F(\text{Br-rich})} = E_{Mn_3Br_8} - (4 \times E_{MnBr_2} - \mu_{\text{Mn-min}})$$

where $E_{Mn_3Br_8}$ and E_{MnBr_2} represent the total energies of the Mn_3Br_8 and $MnBr_2$ monolayers, $\mu_{\text{Mn-max}}$ is the chemical potential of Mn under Mn-rich environment, which is calculated as the energy of Mn atom in its bulk structure, $\mu_{\text{Mn-min}}$ is the chemical potential of Mn under the Br-rich environment, which is calculated as:

$$\mu_{\text{Mn-min}} = E_{MnBr_2} - 2 \times \mu_{\text{Br-max}}$$

where $\mu_{\text{Br-max}}$ is the chemical potential of Br and calculated as the energy of Br atom in gas phase. As shown in Fig. 3c, the formation energies under Mn-rich/Br-rich environment are 6.30/0.71 eV per Mn vacancy, indicating that the formation of Mn vacancy is energetically more favorable under the Br-rich environment. Indeed, the S vacancy has been experimentally achieved in MoS_2 monolayer [56], and the predicted formation energy of S vacancy under the S-rich environment is 2.35 eV [57]. Moreover, structuring porous nano-architecture like β-FeOOH/PNGNs (porous nitrogen-doped graphene networks) can induce significant Fe-vacancy [58], and the Bridgman method was adopted to induce ordering Fe vacancy. We also hope that these methods are applicable for inducing Mn vacancy [59]. Plus, there is no negative frequency found in the phonon spectrum of Mn_3Br_8 monolayer shown in Fig. 5a, proving the dynamical stability. These results approve our design of introducing Mn vacancy to bring in ferromagnetism.

The ferromagnetism of Mn_3Br_8 monolayer attributes to the FM super-exchange interaction. According to the Goodenough–Kanamori–Anderson (GKA) rule [55], super-exchange interaction between the Mn ions is FM when the Mn-Br-Mn angle is around 90°. In such configuration (Additional file 1: Fig. S2), the Mn-d orbital tends

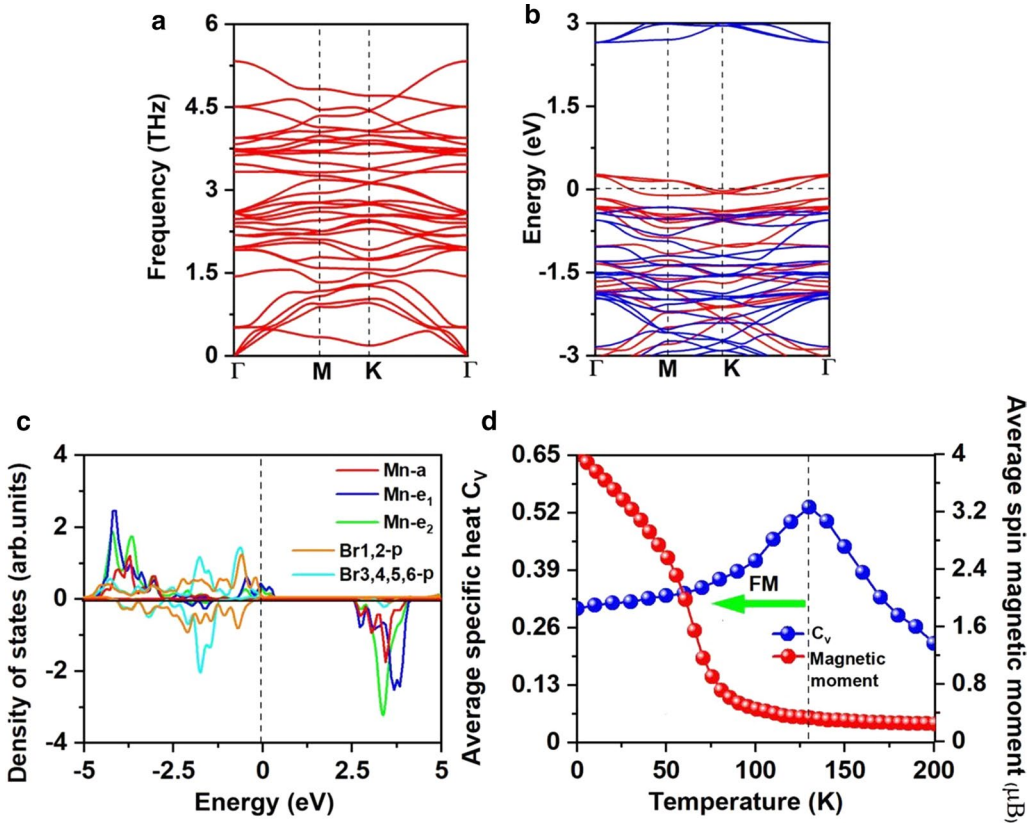

Fig. 5 **a** Phonon spectrums, **b** spin-resolved electronic band structure, and **c** projected density of states (PDOS) of Mn-d orbitals and Br-p orbitals for Mn_3Br_8 monolayer. **d** On-site magnetic moments of Mn atoms and the specific heat C_v as function of temperature based on Heisenberg model for Mn_3Br_8 monolayer. The Fermi level for band structure and PDOS is set as 0 eV

to AFM couples with different orthogonal Br-p orbitals, and thus the indirect Mn–Mn magnetic coupling is expected to be FM. But if each Mn ion has 5 unpaired electrons like $MnBr_2$ monolayer, super-exchange is AFM although the Mn-Br-Mn angle is close to 90° because there are no empty spin-up Mn-d orbitals left in $MnBr_2$ monolayer and spin-up d-electrons cannot hop between the neighboring Mn site [60]. There are existing two different super-exchange interaction paths in Mn_3Br_8 (Fig. 3a), and both are FM. One involves central Br1,2 atoms with Mn-Br bond lengths of 2.76 Å and Mn-Br-Mn angles of 87.5°; the other one involves Br3,4,5,6 atoms with Mn-Br bond length of 2.59 Å and Mn-Br-Mn angles of 95°. The hybridized interactions between p orbitals of Br3,4,5,6 atoms and Mn-d orbitals are stronger than that of p-d hybridization involving Br1,2 atoms, as shown in Fig. 5c, particularly from −2 eV to −1.4 eV. While from 1.4 to −0.9 eV, the *p-d* hybridization involving Br1,2 atoms are dominated.

The bader charge analysis suggests that each Mn atom donates 8/3 electrons to the neighboring Br atoms. Thus, the Mn ions are in the $Mn^{8/3+}$ state. As shown in Fig. 5c, the 13/3 electrons of each Mn ion all fill in the spin-up channel of the d-orbital, while the Br^{1-} ions are in the low-spin state of $4p^6$. Thus, the magnetic moment of each $Mn^{8/3+}$ ion is $13/3\mu_B$; the magnetic moment of Br^{1-} ions are neglectable (Additional file 1: Fig. S1(b)). Inducing ferromagnetism by vacancy can also be observed for the d^0 systems, like ZnS and ZnO [61, 62], single vacancy can induce magnetic moment as large as $2\mu_B$ [61]. For each Mn ion, 2/3 d-orbital is unoccupied; the spin-up channel of both e_1 and e_2 orbitals are partially occupied and crossing the Fermi level, resulting in half-metallicity. The half-metallic character also can be observed from the spin-resolved electronic band structure shown in Fig. 5b. The spin-up channel is metallic, while the spin-down channel is semiconducting with the indirect band gap of 2.97 eV; the VBM/CBM locates at the M/Γ point. The value of the band gap is close to those of the MnP (2.86 eV) [63], MnAs (2.92 eV) [63], and Ni_2NO_2 (2.98 eV) [64], which is large enough to prevent the thermally excited spin-flip. Comparing with the $MnBr_2$ monolayer, both the VBM and CBM of the semiconducting channel get more closer to the Fermi level. The CBM is still dominated by the Mn atoms, while the VBM is dominated by the new Br1,2 atoms. Meanwhile, the semiconducting channel converts from direct to indirect, and the band gap reduces. The similar phenomenon was observed in $MnCl_2$ monolayer with H functionalization [60].

The magnetization directions are determined by the magnetic anisotropy energy (MAE). The MAE of solids arises from two contributors, namely the magneto-crystalline energy (MCE) related to the spin–orbit coupling (SOC) and the magnetic dipolar anisotropy energy (MDE) attributed by the magneto-static dipole–dipole interaction. The MDE in the 3D isotropic materials, such as bcc Fe and fcc Ni, is very small. But for low-dimensional materials composed of transition metal atoms with large magnetic moment, the MDE should not be ignored [65–67]. The MCE is defined as the difference between the magnetization energy along the in-plane (100 or 010) and out-of-plane (001) directions by taking the SOC into account. The MDE is obtained as the difference of E_d between the in-plane and out-of-plane magnetizations. E_d in atomic Rydberg units is given by [65, 66]

$$E_d = \sum_{ij} \frac{2m_i m_j}{c^2} M_{ij}$$

where the speed of light, $c = 274.072$, i/j are the atomic position vectors in the unit cell, and m_i/m_j is the atomic magnetic moment (μ_B) on site i/j. The magnetic dipolar Madelung constant M_{ij} is calculated via

$$M_{ij} = \sum_R \frac{1}{|R+i+j|^3} \left\{ 1 - 3 \frac{\left[(R+i+j)\cdot \hat{m}_i\right]^2}{|R+i+j|^2} \right\}$$

where R are the lattice vectors. In a 2D material, since all the R and i are in-plane, the second term would be zero for the out-of-plane magnetization, resulting in the positive M_{ij}, while M_{ij} is negative for an in-plane magnetization [67]. Therefore, the MDE relates to the magnetic moment of transition metal and always prefers the in-plane magnetization.

The calculated MCE for Mn_3Br_8 monolayer is −1.90 meV per formula unit (Fig. 6a), much larger than those of bulk Fe (0.001 meV per atom), and Ni (0.003 meV per atom) [68], and larger than that of the Fe monolayer on Rh (111) (0.08 meV per atom) [69], suggesting that the magnetization of the Mn_3Br_8 monolayer is thermal stable. The relationship between the MCE and the azimuthal angle can be described by the following equation [70]:

$$\mathrm{MCE}(\theta) = A\cos^2(\theta) + B\cos^4(\theta)$$

where A and B are the anisotropy constants and θ is the azimuthal angle. The fitting result is shown in Additional file 1: Figs. S3. Additionally, the evolution of MCE with the spin axis rotating through the whole space is illustrated in Fig. 6b. MCE within the xy plane shows no difference, but reaches the maximum value along the direction perpendicular to the xy plane, confirming the

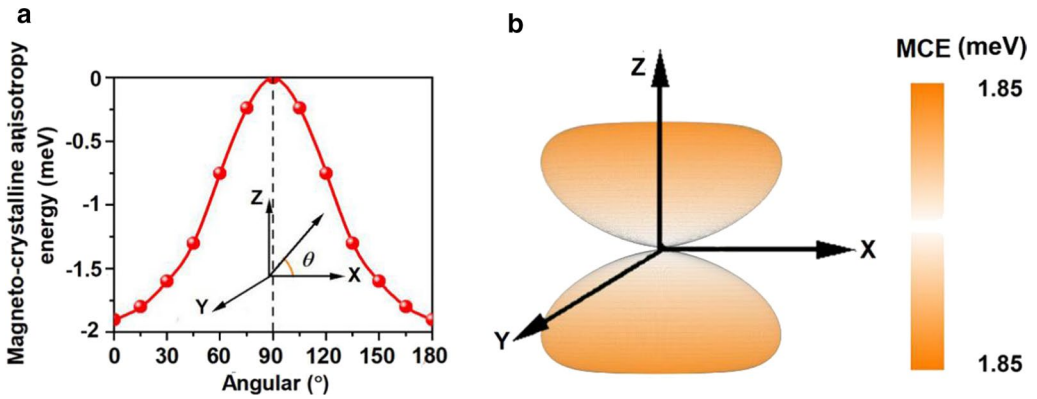

Fig. 6 Variation of magneto-crystalline anisotropy energy (MCE) **a** with respect to azimuthal angle and **b** in the space for Mn_3Br_8 monolayer

strong magnetic anisotropy. The MDE is −0.43 meV per formula unit, and MAE (MCE + MDE) is −2.33 meV per formula unit. The negative value indicates that the easy magnetization axis is along the in-plane directions. The MDE does not change the magnetization direction, but enhances it. Additionally, the MAE of Mn_3Br_8 monolayer is much larger than that of $MnBr_2$ monolayer, proving again the effectiveness of our design.

We further calculated the T_c for FM Mn_3Br_8 monolayer by performing the Monte Carlo (MC) simulations based on the Heisenberg model, which has been proven to be the effective method for predicting T_c for 2D materials [11, 15, 48, 58, 71–76]. Our estimated T_c of CrI_3 monolayer is 42 K (Additional file 1: Fig. S4) [76], agreeing well with the experimental measured value [2] and previous calculation results [15, 58, 71, 72, 74, 76], which proves the accuracy of our adopted method. The spin-Hamiltonian including the nearest neighboring (NN) magnetic interaction is described as

$$H = -\sum_{i,j} JM_iM_j$$

where J is the NN magnetic exchange parameter, $M_{i/j}$ is the magnetic moment of Mn ions and integral close to the number of the spin polarized electrons based on Monte Carlo method [71, 77, 78], i and j stand for the NN pair of Mn ions. The magnetic coupling parameter J is calculated via the energy difference between the FM and AFM states as

$$J = \frac{E_{\mathrm{AFM1}} - E_{\mathrm{FM}}}{16M^2}$$

The calculated J of NN Mn ions is 1.01 meV; the positive value indicates the preferring of FM coupling.

The calculated J of the NN Mn ions and the $100 \times 100 \times 1$ supercell containing 20,000 magnetic moment vectors were adopted to perform the MC simulations. The simulations at each temperature lasts for 10^5 steps. Each magnetic moment vector rotates randomly in all directions. Figure 5d shows the evolution of specific heat defined as $C_V = \left(\langle E^2\rangle - \langle E\rangle^2\right)/K_BT^2$ with temperature, from which we obtained the T_c of 130 K for Mn_3Br_8 monolayer by locating the peak position of C_v, higher than the liquid-nitrogen temperature (77 K), and T_c of CrI_3 (45 K) [2] and $Cr_2Ge_2Te_6$ (28 K) [3], CrX_3 (X = F, Cl, Br) (36 ~ 51 K) [11], $CrXTe_3$ (X = Si, Ge) (35.7 K, 57,2 K) [48]. Our calculations demonstrate that the FM Mn_3Br_8 monolayer has the large MAE and Curie temperature higher than the liquid-nitrogen temperature.

Mn_3Br_8 monolayer under biaxial strain and carrier doping

Strain engineering has been proven applicable for many 2D materials, and effective to alter the structural parameters, such as the bond lengths and angles, and tune the electronic and magnetic properties. In this context, we investigated Mn_3Br_8 monolayer under the biaxial strain ranging from −5% to 5%. It turns out that Mn_3Br_8 monolayer under biaxial strain from −5 to 5% maintains to be FM and the atomic magnetic moment hardly changes. As shown in Figs. 7a and c, the angles between two Mn atoms and Br1,2 atoms ($\theta_{\text{Mn-Br1,2-Mn}}$) are 84°–90°, which increases as the strain and gradually approaches 90°. The Mn–Br–Mn angles involving Br3,4,5,6 atoms ($\theta_{\text{Mn-Br3,4,5,6-Mn}}$) gradually deviate from 90°, ranging from 90° to 100°. Thus, super-exchange interactions between the Mn ions mediated via different orthogonal Br-p orbitals are still FM.

Both the Mn–Mn and Mn-Br distances increase monotonically as the strain changing from –5% to 5%. Correspondingly, the exchange parameter under the biaxial strain presented in Fig. 8a decreases with the biaxial strain changing from –5% to 5% and reach the largest value (1.18 meV) under –5% biaxial strain. The Curie

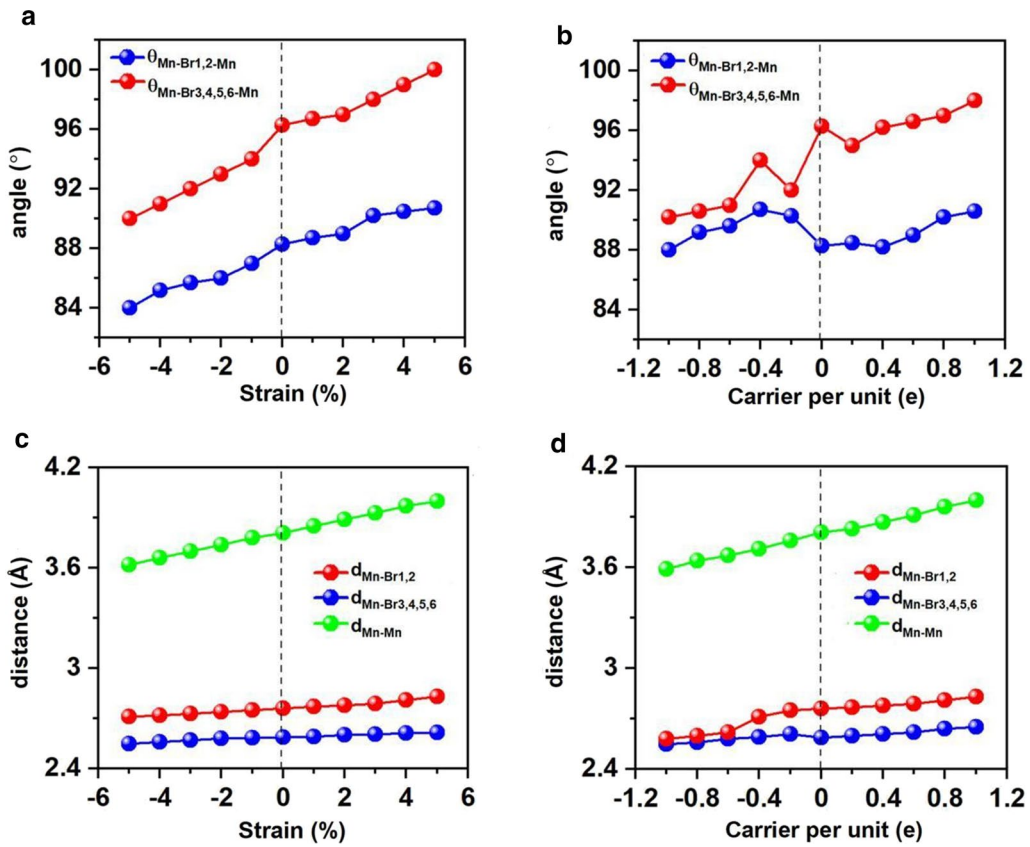

Fig. 7 Variations of angles between two Mn and Br atoms, the distance between Mn and Br atoms, and distance between nearest neighboring Mn atoms with respect to the applied biaxial strain and carrier doping. Variation of **a** angle and **c** distance with respect to biaxial strain, variations of **b** angle and **d** distance with respect to carrier doping. Positive and negative values of carrier doping represent the electron and hole doping, respectively

temperature of Mn_3Br_8 monolayer under −5% biaxial strain is 160 K (Fig. 9a). Particularly, the Mn-Br bonds under the increasing tensile strain become longer, and the angles of Mn-Br3,4,5,6-Mn deviate from 90°, which are the main reason why the FM super-exchange interaction becomes weaker. Consequently, the Curie temperature decreases. It is similar with $CrPTe_3$ and $FePS_3$ monolayers [79]. Additionally, the MDE decreases with the increasing strain (Additional file 1: Fig. S5(b)); the MAE under −1% biaxial strain is the largest (−3.04 meV). The −5–5% strain does not cause large structural deformation for Mn_3Br_8 monolayer, and the morphology of its band structures hardly changes. Mn_3Br_8 monolayer keeps to be half-metallic. Both VBM and CBM in the semiconducting spin-channel move upward slightly to the higher energy as shown in Figs. 8c and 10; the band gap increases slowly with the increasing biaxial strain to 3.12 eV under 5% biaxial strain.

Electron/hole doping always leads to VBM/CBM moving away from the Fermi level. Our calculations show that Mn_3Br_8 monolayer with −1–1e ($\sim 1.7 \times 10^{14} cm^{-2}$) carrier doping per formula unit is still FM; the atomic magnetic moment of each Mn ion is still $13/3\mu_B$. As shown in Fig. 7b and d, with carrier doping from −1e to 1e per formula unit, the Mn-Br-Mn angles involving Br3,4,5,6 atoms are about 90° ~ 98°; the Mn-Br1,2-Mn angles are about 88° ~ 90°. The Mn–Mn and Mn-Br1,2 distances increase with the increasing electron doping. Mn_3Br_8 monolayer with 0.2e and 0.4e carrier doping has larger magnetic exchange parameter (Fig. 8a). The Curie temperature at 0.2e electron doping is largest of 140 K (Fig. 9b). Additionally, with −1e ~ 0.2e doping, the MAE is along in-plane directions; the MDE decreases with the increasing electron doping. Under 0.4e doping, the MCE turns to be positive with the value of 0.41 meV per formula unit; the MAE is only 0.01 meV per formula unit with taking the MDE into account (Additional file 1: Figs. S5(a) and (b)). With 0.6e, 0.8e and 1e doping, the PMA (perpendicular magnetic anisotropy energy) is 1.70, 2.42, and 5.13 meV, respectively, large enough for spintronic applications (Fig. 8b).

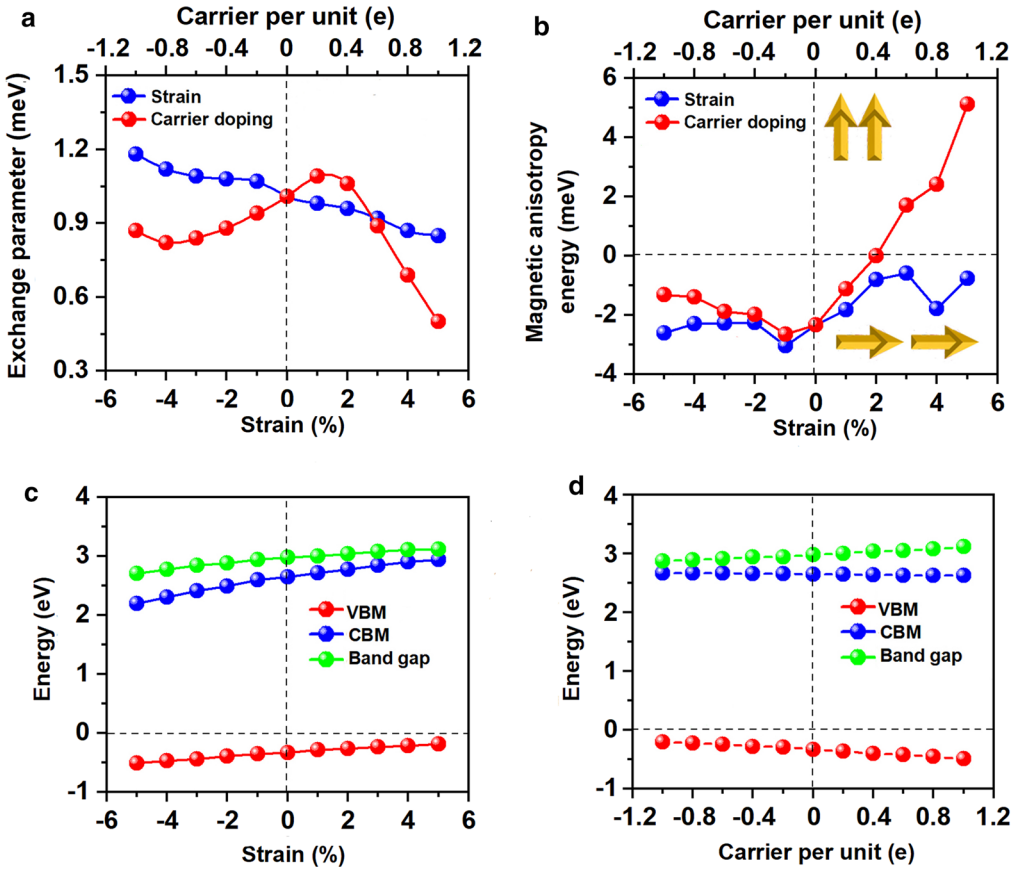

Fig. 8 Variations of **a** the exchange parameter and **b** magnetic anisotropy energy (MAE) for Mn_3Br_8 monolayer with respect to the applied biaxial strain and carrier doping. The variations of valence band maximum (VBM), conduction band minimum (CBM), and band gap in the semiconducting channel for Mn_3Br_8 monolayer with respect to **c** the applied biaxial strain and **d** carrier doping ranging. Positive and negative values of the carrier doping represent the electron and hole doping, respectively

Additionally, Mn_3Br_8 monolayer with carrier doping of −1e ~ 1e per formula unit maintains to be half-metallic. Its band gap in the semiconducting spin-channel increases/decreases slightly with the increasing electron/hole doping as shown in Fig. 8d; the positions of the VBM and CBM do not change. Exceptional, Mn_3Br_8 monolayer turns to be FM spin-gapless semiconductors (SGS) with the metallic spin-channel opening up a very small energy gap (0.07 eV) under −0.6e and −0.8e hole doping; its Fermi level locates in the band gap region (Fig. 11b and c, more clearly figures are presented in Additional file 1: Figs. S6(a) and (b)). Correspondingly, electrons may be easily excited from the valence band to the conduction band with a small input of energy, which simultaneously produces 100% spin polarized electron and hole carriers. The Curie temperature at −0.6e and −0.8e hole doping is 110 K (Fig. 9c and d), higher than liquid-nitrogen temperature (77 K). Considering with that the charge density modulation of $10^{13} \sim 10^{15} cm^{-2}$ was already achieved experimentally [80–82], our predicted properties of Mn_3Br_8 monolayer with carrier doping are also experimentally approachable.

Conclusions

In summary, the stability, electronic, and magnetic properties of Mn_3Br_8 monolayer have been carefully investigated. Our results show that Mn_3Br_8 monolayer is FM half-metal with 130 K Curie temperature and with 2.97 eV band gap for the semiconducting spin-channel. Plus, the magnetic moment of each Mn ion is $13/3\mu_B$; the MAE is −2.33 meV per formula unit. The Mn_3Br_8 monolayer is designed by inducing single Mn vacancy in the $2 \times 2 \times 1$ supercell of $MnBr_2$ monolayer to break the AFM coupling d^5 configuration. The feasibility of forming the Mn vacancy and the dynamical, mechanical stability of Mn_3Br_8 monolayer have been comprehensively confirmed. Additionally, Mn_3Br_8 monolayer under biaxial strain −5% ~ 5% is still FM half-metal with 2.71 ~ 3.12 eV band gap for the semiconducting spin-channel, whose Curie temperature

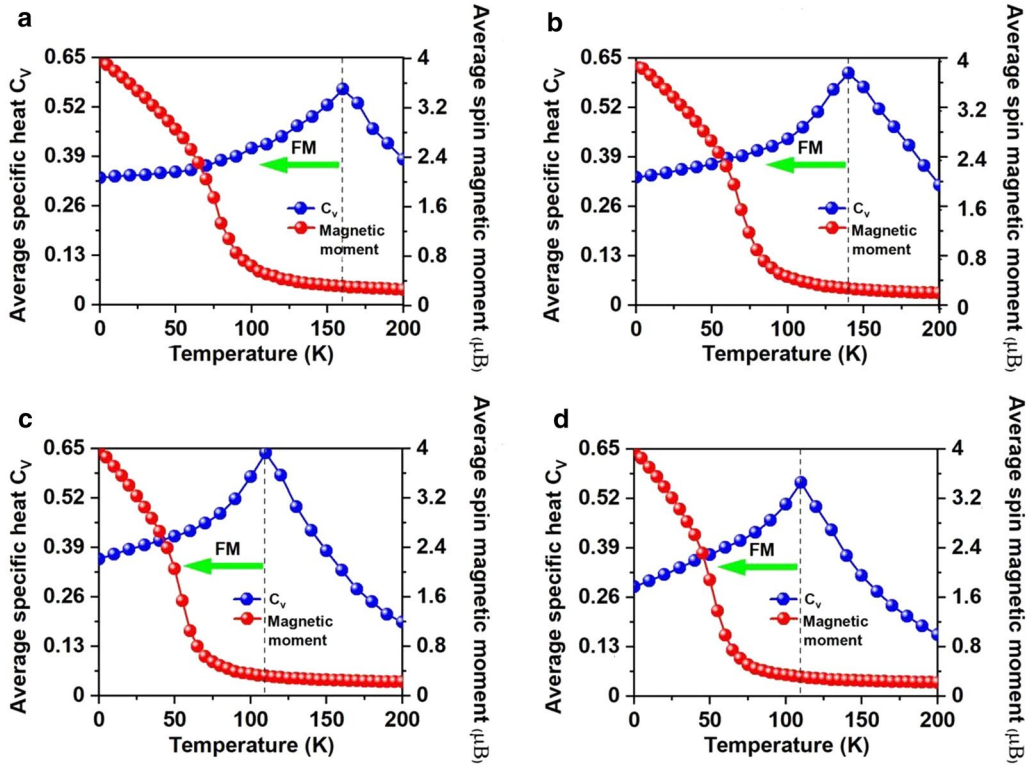

Fig. 9 On-site magnetic moments of Mn atoms and the specific heat C_v as function of temperature based on Heisenberg model for Mn_3Br_8 monolayer **a** under -5% biaxial strain, with **b** 0.2e, **c** -0.6e, and **d** -0.8e carrier doping per formula unit. Positive and negative values represent the electron and hole doping, respectively

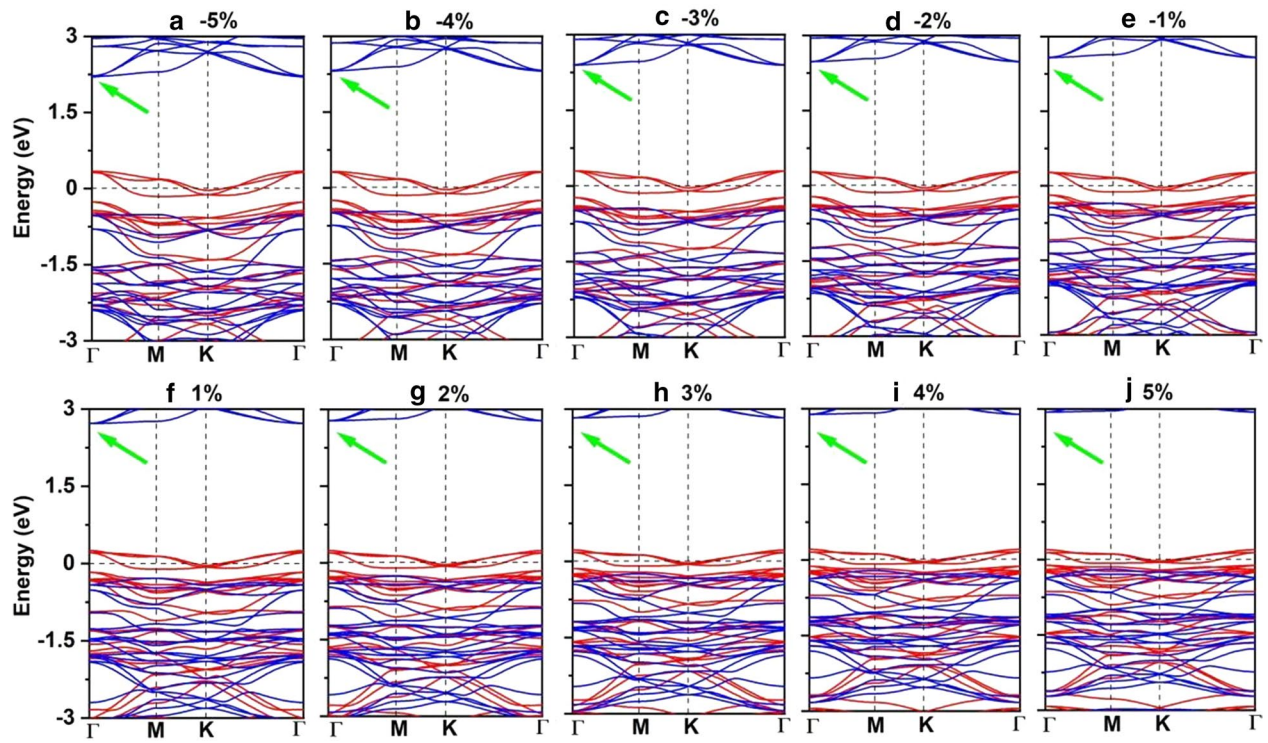

Fig. 10 **a**–**j** Spin-resolved band structure for Mn_3Br_8 monolayer under biaxial strain from -5% to 5%. The green arrow denotes the indirect band gap

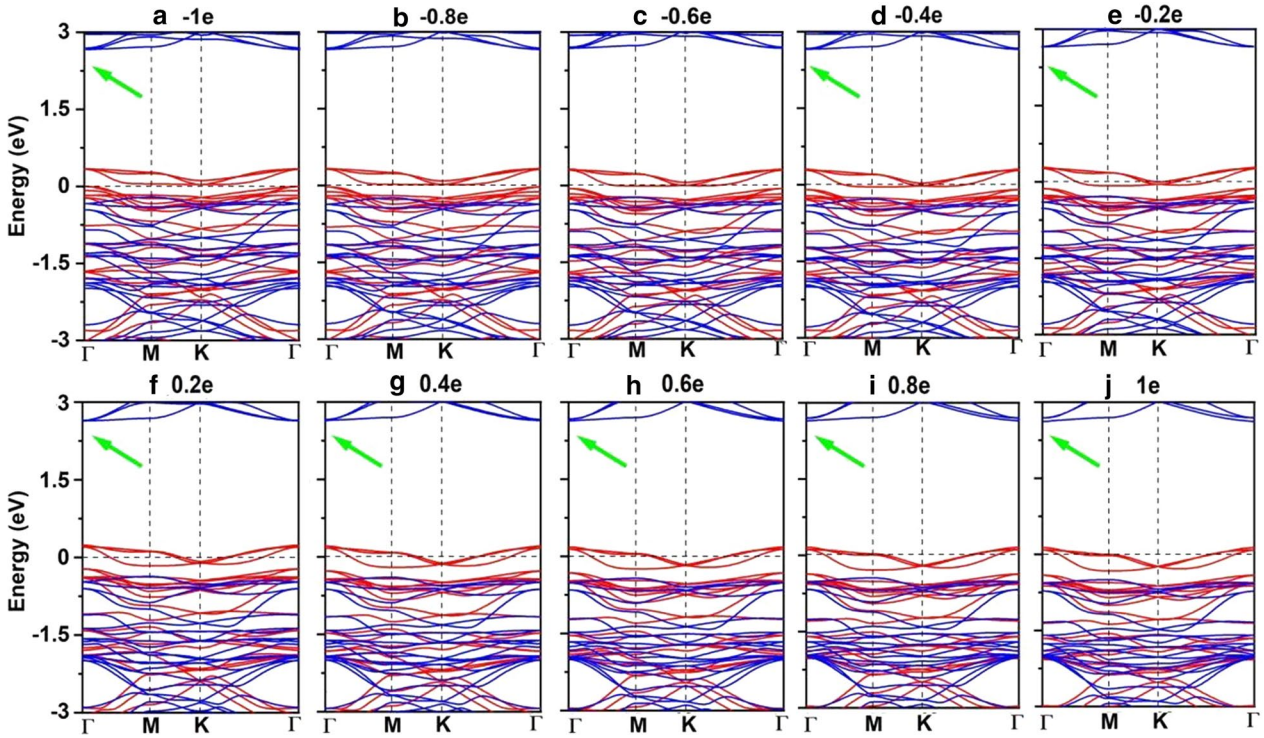

Fig. 11 **a–j** Spin-resolved band structure for Mn_3Br_8 monolayer with carrier doping from -1e to 1e per formula unit. Positive and negative values represent the electron and hole doping, respectively. The green arrow denotes the indirect band gap

under −5% biaxial strain is 160 K. Both biaxial strain and carrier doping make the MAE increase, which turns to be perpendicular to the plane under electron doping. With 0.8e and 0.6e hole doping, Mn_3Br_8 monolayer turns to be spin-gapless semiconductor (SGS) with band gap of 0.07 eV. Our calculations demonstrate Mn_3Br_8 monolayer as FM half-metal with high Curie temperature, and having large MAE and large magnetic moment, and tunable electronic and magnetic properties under the applied biaxial strain and carrier doping.

Abbreviations

2D: Two-dimensional; AFM: Antiferromagnetic; CBM: Conduction band minimum; DFT: Density functional theory; DOS: Density of states; FIM: Ferrimagnetic; FM: Ferromagnetic; GGA: Generalized gradient approximation; GKA: Goodenough–Kanamori–Anderson; MAE: Magnetic anisotropy energy; MCE: Magneto-crystalline anisotropy energy; MC: Monte Carlo; MDE: Magnetic dipolar anisotropy energy; MTJ: Magnetic tunneling junctions; NM: Non-magnetic; NN: Nearest neighboring; PAW: Projector augmented wave; PBE: Perdew–Burke–Ernzerhof; PMA: Perpendicular magnetic anisotropy energy; PNGN: Porous nitrogen-doped graphene networks; SGS: Spin-gapless semiconductor; SOC: Spin–orbit coupling; VASP: Vienna ab-initio simulation package; VBM: Valence band maximum; VDW: Van der Waals.

Supplementary information

The online version contains supplementary material available at https://doi.org/10.1186/s11671-021-03523-0.

Additional file 1. Revised supporting information.

Acknowledgements

Not applicable

Authors' contributions

YH designed the study, performed the research and drafted the original manuscript, SJ, ZFL, HHZ, and JHW participated in part of research, XLF supervised the study, and revised the original and revised manuscript. All authors read and approved the final manuscript.

Funding

This work was supported by the National key R&D Program of China (2018YFB0703800), the Natural Science Fund of Shaanxi Province for distinguished Young Scholars (2019JC-10) and Key Project (2021JZ-07), the Polymer Electromagnetic Functional Materials Innovation Team of Shaanxi Sanqin Scholars, and sponsored by the seed Foundation of Innovation and Creation for Graduate Students (CX2020083) in Northwestern Polytechnical University.

Availability of data and materials

The datasets generated during and/or analyzed during the current study are available from the corresponding author on reasonable request.

Declaration

Competing interests
The authors declare that they have no competing interests.

Author details
[1]State Key Laboratory of Solidification Processing, Center for Advanced Lubrication and Seal Materials, School of Material Science and Engineering, Northwestern Polytechnical University, 127 YouYi Western Road, Xi'an 710072, Shaanxi, China. [2]Queen Mary University of London Engineering School, Northwestern Polytechnical University, 127 YouYi Western Road, Xi'an 710072, Shaanxi, China.

Received: 4 January 2021 Accepted: 4 April 2021
Published online: 29 April 2021

References

1. Fert A (2008) Nobel Lecture: Origin, development, and future of spintronics. Rev Mod Phys 80:1517
2. Huang B, Clark G, Navarro-Moratalla E, Klein DR, Cheng R, Seyler KL, Zhong D, Schmidgall E, McGuire MA, Cobden DH, Yao W, Xiao D, Jarillo-Herrero P, Xu X (2017) Layer-dependent ferromagnetism in a van der waals crystal down to the monolayer limit. Nature 546:270
3. Gong C, Li L, Li Z, Ji H, Stern A, Xia Y, Cao T, Bao W, Wang C, Wang Y, Qiu ZQ, Cava RJ, Louie SG, Xia J, Zhang X (2017) Discovery of intrinsic ferromagnetism in two-dimensional van der waals crystals. Nature 546:265
4. Gong C, Zhang X (2019) Two-dimensional magnetic crystals and emergent heterostructure devices. Science 363:706
5. Lu SH, Zhou QH, Guo YL, Zhang YH, Wu YL, Wang JL (2020) Coupling a crystal graph multilayer descriptor to active learning for rapid discovery of 2D ferromagnetic semiconductors/half-metals/metals. Adv Mater 32:2002658
6. Lee JW, Ko TY, Kim JH, Bark HY, Kang B, Jung SG, Park T, Lee Z, Ryu S, Lee C (2017) Structural and optical properties of single- and few-layer magnetic semiconductor $CrPS_4$. ACS Nano 11:10935
7. Cui FF, Zhao XX, Xu JJ, Tang B, Shang QY, Xing JP, Huan YH, Liao JH, Chen Q, Hou YL, Controlled growth and thickness-dependent conduction-type transition of 2D ferrimagnetic Cr_2S_3 semiconductors. Adv Mater 32:1905896.
8. Yu S, Wang Y, Song YZ, Xia L, Yang XL, Fang H, Li QL, Li XG (2021) Hole doping induced half-metallic itinerant ferromagnetism and giant magnetoresistance in CrI_3 monolayer. Appl Surf Sci 535:147693
9. Deng YJ, Yu YJ, Song YC, Zhang JZ, Wang NZ, Sun ZY, Yi YF, Wu YF, Wu SW, Zhu JY, Wang J, Chen XH, Zhang YB (2018) Gate-tunable room-temperature ferromagnetism in two-dimensional Fe_3GeTe_2. Nature 563:94
10. Zhuang HL, Kent PRC, Hennig RG (2016) Strong anisotropy and magnetostriction in the two-dimensional Stoner ferromagnet Fe_3GeTe_2. Phys Rev B 93:134407
11. Zhang WB, Qu Q, Zhu P, Lam CH (2015) Robust intrinsic ferromagnetism and half semiconductivity in stable two-dimensional single-layer chromium trihalides. J Mater Chem C 3:12457
12. Ma AN, Wang PJ, Zhang CW (2020) Intrinsic ferromagnetism with high temperature, strong anisotropy and controllable magnetization in the CrX (X=P, As) monolayer. Nanoscale 12:5464
13. Han RL, Yan JY (2020) Prediction of novel 2D intrinsic ferromagnetic materials with high Curie temperature and large perpendicular magnetic anisotropy. J Phys Chem C 124:7956
14. Zhuang HL, Xie Y, Kent PRC, Ganesh P (2015) Computational discovery of ferromagnetic semiconducting single-layer $CrSnTe_3$. Phys Rev B 92:035407
15. Huang CX, Feng JS, Wu F, Ahmed D, Huang B, Xiang HJ, Deng KM, Kan EJ (2018) Toward intrinsic room-temperature ferromagnetism in two-dimensional semiconductors. J Am Chem Soc 140:11519
16. Botana AS, Norman MR (2019) Electronic structure and magnetism of transition metal dihalides: Bulk to monolayer. Phys Rev Mater 3:044001
17. Kumar H, Frey NC, Dong L, Anasori B, Gogotsi Y, Shenoy VB (2017) Tunable magnetism and transport properties in Nitride MXenes. ACS Nano 11:7648
18. Lin SH, Kuo JL (2014) Towards the ionic limit of two-dimensional materials: monolayer alkaline earth and transition metal halides. Phys Chem Chem Phys 16:20763
19. Kong T, Stolze K, Timmons EI, Tao J, Ni D, Guo S, Yang Z, Prozorov R, Cava RJ (2019) VI_3-a new layered ferromagnetic semiconductor. Adv Mater 31:1808074
20. Wu SM, Zhang W, Borisov P, Pearson JE, Jiang JS, Lederman D, Hoffmann A, Bhattacharya A (2016) Antiferromagnetic spin seebeck effect. Phys Rev Lett. 116:097204
21. Kim HH, Yang B, Patel T, Sfigakis F, Li C, Tian S, Lei H, Tsen AW (2018) One million percent tunnel magnetoresistance in a magnetic van der waals heterostructure. Nano Lett 18:4885
22. He JJ, Li X, Lyu P, Nachtigall P (2017) Near-room-temperature Chern insulator and Dirac spin-gapless semiconductor: nickel chloride monolayer. Nanoscale 9:2246
23. Hu H, Tong WY, Shen YH, Wan XG, Duan CG (2020) Concepts of the half-valley-metal and quantum anomalous valley Hall effect. npj Comput Mater 6:129.
24. Huang CX, Du YP, Wu HP, Xiang HJ, Deng KM, Kan EJ (2018) Prediction of intrinsic ferromagnetic ferroelectricity in a transition-metal halide monolayer. Phys Rev Lett 120:147601
25. Wollan EO, Koehler WC, Wilkinson MK (1958) Neutron diffraction study of the magnetic properties of $MnBr_2$. Phys Rev 110:638
26. Kulish VV, Huang W (2017) Single-layer metal halides MX_2 (X=Cl, Br, I): stability and tunable magnetism from first principles and Monte Carlo simulations. J Mater Chem C 5:8734
27. Hu Y, Gong YH, Zeng HH, Wang JH, Fan XL (2020) Two-dimensional stable Fe-based ferromagnetic semiconductors: FeI3 and FeI1.5Cl1.5 monolayers. Phys Chem Chem Phys 22:24506
28. Marozau I, Das PT, Döbeli M, Storey JG, Uribe-Laverde MA, Das S, Wang C, Rössle M, Bernhard C (2014) Influence of La and Mn vacancies on the electronic and magnetic properties of $LaMnO_3$ thin films grown by pulsed laser deposition. Phys Rev B 89:174422
29. Zhou W, Zou X, Najmaei S, Liu Z, Shi Y, Kong J, Lou J, Ajayan PM, Yakobson BI, Idrobo JC (2013) Intrinsic structural defects in monolayer molybdenum disulfide. Nano Lett 13:2615
30. Conley HJ, Wang B, Ziegler JI, Haglund RF, Pantelides ST, Bolotin KI (2013) Bandgap engineering of strained monolayer and bilayer MoS_2. Nano Lett 13:3626
31. He K, Poole C, Mak KF, Shan J (2013) Experimental demonstration of continuous electronic structure tuning via strain in atomically thin MoS_2. Nano Lett 13:2931
32. Wang Y, Cong C, Yang W, Shang J, Peimyoo N, Chen Y, Kang J, Huang W, Yu T (2015) Strain-induced direct–indirect bandgap transition and phonon modulation in monolayer WS_2. Nano Res 8:2562
33. Hui YY, Liu X, Jie W, Chan NY, Hao J, Hsu YT, Li LJ, Guo W, Lau SP (2013) Exceptional tunability of band energy in a compressively strained trilayer MoS_2 sheet. ACS Nano 7:7126
34. Plechinger G, Gomez AG, Buscema M, VanderZant HSJ, Steele GA, Kuc A, Heine T, Schüller C, Korn T (2015) Control of biaxial strain in single-layer molybdenite using local thermal expansion of the substrate. 2D Mater 2:015006
35. Gomez AC, Roldán R, Cappelluti E, Buscema M, Guinea F, Van der Zant HSJ, Steele GA (2013) Local strain engineering in atomically thin MoS_2. Nano Lett 13:5361
36. Roldán R, Gomez AC, Cappelluti E, Guinea F (2015) Strain engineering in semiconducting two-dimensional crystals. J Phys Condensed Matter 27:313201
37. Wang Z, Zhang TY, Ding M, Dong BJ, Li YX, Chen ML, Li XX, Huang JQ, Wang HW, Zhao XT, Li Y, Chen D, Yang T, Zhang J, Ono SP, Han Z, Zhang ZD (2018) Electric-field control of magnetism in a few-layered van der Waals ferromagnetic semiconductor. Nat Nanotech 13:554
38. Jiang S, Li L, Wang Z, Mak KF, Shan J (2018) Controlling magnetism in 2D CrI_3 by electrostatic doping. Nat Nanotech 13:549
39. Kresse G, Furthmüller J (1996) Efficient iterative schemes for ab initio total-energy calculations using a plane-wave basis set. Phys Rev B 54:11169
40. Blöchl PE (1994) Projector augmented-wave method. Phys Rev B 50:17953
41. Kresse G, Joubert D (1999) From ultrasoft pseudopotentials to the projector augmented-wave method. Phys Rev B 59:1758

42. Perdew JP, Burke K, Ernzerhof M (1996) Generalized gradient approximation made simple. Phys Rev Lett 77:3865
43. Liechtenstein AI, Anisimov VI, Zaanen J (1995) Density-functional theory and strong interactions: orbital ordering in Mott-Hubbard insulators. Phys Rev B 52:R5467
44. Zhou J, Sun Q (2011) Magnetism of phthalocyanine-based organometallic single porous sheet. J Am Chem Soc 133:15113
45. Monkhorst HJ, Pack JD (1976) Special points for Brillouin-zone integrations. Phys Rev B 13:5188
46. Parlinski K, Li Z, Kawazoe Y (1997) First-principles determination of the soft mode in cubic ZrO_2. Phys Rev Lett 78:4063
47. Liu J, Sun Q, Kawazoe Y, Jena P (2016) Exfoliating biocompatible ferromagnetic Cr-trihalide monolayers. Phys Chem Chem Phys 18:8777
48. Li XX, Yang JL (2014) $CrXTe_3$ (X = Si, Ge) nanosheets: two dimensional intrinsic ferromagnetic semiconductors. J Mater Chem C 2:7071
49. Li XX, Wu XJ, Yang JL (2014) Half-metallicity in $MnPSe_3$ exfoliated nanosheet with carrier doping. J Am Chem Soc 136:11065
50. Grimme S (2006) Semiempirical GGA-type density functional constructed with a long-range dispersion correction. J Comput Chem 27:1787
51. Bucko T, Hafner J, Lebegue S, Angyan JG (2010) Improved description of the structure of molecular and layered crystals: ab initio DFT calculations with van der Waals corrections. J Phys Chem A 114:11814
52. Zacharia R, Ulbricht H, Hertel T (2004) Interlayer cohesive energy of graphite from thermal desorption of polyaromatic hydrocarbons. Phys Rev B 69:155406
53. Cadelano E, Palla PL, Giordano S, Colombo L (2010) Elastic properties of hydrogenated graphene. Phys Rev B 82:235414
54. Bertolazzi S, Brivio J, Kis A (2011) Stretching and breaking of ultrathin MoS_2. ACS Nano 5:9703
55. Stöhr J, Siegmann HC (2006) Magnetism: from fundamentals to nanoscale dynamics. Springer, New York
56. Lin Z, Carvalho BR, Kahn E, Lv R, Rao R, Terrones H, Pimenta MA,Terrones M (2016) Defect engineering of two-dimensional transition-metal dichalcogenides. 2D Mater 3:022002.
57. Liu D, Guo Y, Fang L, Robertson J (2013) Sulfur vacancies in monolayer MoS_2 and its electrical contacts. Appl Phys Lett 103:183113
58. Li Y, Huang JH, Hu X, Bi LL, Cai PW, Jia JC, Chai CL, Wei SQ, Dai LM, Wen ZH (2018) Fe vacancies induced surface FeO_6 in nanoarchitectures of N-doped graphene protected β-FeOOH: effective active sites for pH-universal electrocatalytic oxygen reduction. Adv Funct Mater 28:1803330
59. Wang DM, He JB, Xia TL, Chen GF (2011) Effect of varying iron content on the transport properties of the potassium-intercalated iron selenide $K_xFe_{2-y}Se_2$. Phys Rev B 83:132502
60. Farooq MU, Khan I, Moaied M, Hong JS (2017) Hydrogen functionalization induced two-dimensional ferromagnetic semiconductor in Mn di-halide systems. Phys Chem Chem Phys 19:29516
61. Zhang ZK, Schwingenschlögl U, Roqan IS (2014) Possible mechanism for d^0 ferromagnetism mediated by intrinsic defects. RSC Adv 4:50759
62. Aravindh SDA, Schwingenschlögl U, Roqan IS (2015) Defect induced d^0 ferromagnetism in a ZnO grain boundary. J Chem Phys 143:224703
63. Wang B, Zhang YH, Ma L, Wu QS, Guo YL, Zhang XW, Wang JL (2019) MnX (X=P, As) monolayers: a new type of two-dimensional intrinsic room temperature ferromagnetic half-metallic material with large magnetic anisotropy. Nanoscale 11:4204
64. Wang G, Liao Y (2017) Theoretical prediction of robust and intrinsic half-metallicity in Ni_2N MXene with different types of surface terminations. Appl Surf Sci 426:371
65. Tung JC, Guo GY (2007) Systematic *ab initio* study of the magnetic and electronic properties of all 3d transition metal linear and zigzag nanowires. Phys Rev B 76:094413
66. Guo GY, Temmerman W, Ebert H (1991) First-principles determination of the magnetization direction of Fe monolayer in noble metals. J Phys Condens Matter 3:8205
67. Fang Y, Wu S, Zhu ZZ, Guo GY (2018) Large magneto-optical effects and magnetic anisotropy energy in two-dimensional $Cr_2Ge_2Te_6$. Phys Rev B 98:125416
68. Daalderop GHO, Kelly PJ, Schuurmans MFH (1990) First-principles calculation of the magnetocrystalline anisotropy energy of iron, cobalt, and nickel. Phys Rev B 41:11919
69. Luhnert A, Dennler S, Błoński P, Rusponi S, Etzkorn M, Moulas G, Bencok P, Gambardella P, Brune H, Hafner J (2010) Magnetic anisotropy of Fe and Co ultrathin films deposited on Rh(111) and Pt(111) substrates: An experimental and first-principles investigation. Phys Rev B 82:094409
70. Buschow KHJ, Boer FRD (2003) Physics of magnetism and magnetic materials. Kluwer Academic, New York
71. Wu QS, Zhang YH, Zhou QH, Wang JL, Zeng XC (2018) Transition-Metal dihydride monolayers: a new family of two-dimensional ferromagnetic materials with intrinsic room-temperature half-metallicity. J Phys Chem Lett 9:4260
72. Guo YL, Zhang YH, Yuan SJ, Wang B, Wang JL (2018) Chromium sulfide halide monolayers: intrinsic ferromagnetic semiconductors with large spin polarization and high carrier mobility. Nanoscale 10:18036
73. Sun YJ, Zhuo ZW, Wu XJ (2018) Bipolar magnetism in a two-dimensional NbS_2 semiconductor with high Curie temperature. J Mater Chem C 6:11401
74. Wang B, Zhang XW, Zhang YH, Yuan SJ, Guo YL, Dong S, Wang JL (2020) Prediction of a two-dimensional high-Tc f-electron ferromagnetic semiconductor. Mater Horiz 7:1623
75. Li XX, Yang JL (2019) Realizing two-dimensional magnetic semiconductors with enhanced Curie temperature by antiaromatic Ring based organometallic frameworks. J Am Chem Soc 141:109
76. Hu Y, Liu XY, Shen ZH, Luo ZF, Chen ZG, Fan XL (2020) High Curie temperature and carrier mobility of novel Fe. Co and Ni Carbide MXenes Nanoscale 12:11627
77. Wang B, Wu QS, Zhang YH, Guo YL, Zhang XW, Zhou QH, Dong S, Wang JL (2018) High Curie-temperature intrinsic ferromagnetism and hole doping-induced half-metallicity in two-dimensional scandium chlorine monolayers. Nanoscale horiz 3:551
78. Jiang Z, Wang P, Jiang X, Zhao JJ (2018) MBene (MnB): a new type of 2D metallic ferromagnet with high Curie temperature. Nanoscale Horiz 3:335
79. Chittari BL, Park YJ, Lee D, Han M, MacDonald AH, Hwang E, Jung J (2016) Electronic and magnetic properties of single-layer MPX_3 metal phosphorous trichalcogenides. Phys Rev B 94:184428
80. Dhoot AS, Israel C, Moya X, Mathur ND, Friend RH (2009) Large electric field effect in electrolyte-gated manganites. Phys Rev Lett 102:136402
81. Yuan H, Shimotani H, Tsukazaki A, Ohtomo A, Kawasaki M, wasa Y, (2009) High-density carrier accumulation in ZnO field-effect transistors gated by electric double layers of ionic liquids. Adv Funct Mater 19:1046
82. Jiang SW, Li LZ, Wang ZF, Mak KF, Shan J (2018) Controlling magnetism in 2D CrI_3 by electrostatic doping. Nat Nanotech 1:549

Publisher's Note